communications physics

A Nature Portfolio journal

Article

https://doi.org/10.1038/s42005-025-02009-0

Crossover scaling of structural and mechanical properties in 3D assemblies of non-spherical, frictional particles

Dian Fan[1,2] ✉, Yuanyuan Tang[1], Pengfei Wang[3,4,5], Yun Li[3,4,5], Cheng Lian[6], Alberto Striolo[7], Yiqi Chen[8], Zhuojian Lv[1], Jiangpeng Li[1,9], Shuai Zhao[10], Jiaming Bai[10], Ling Zhou[11], Paolo Malgaretti[12], Jinlong Zhu[3,4,5,8] ✉ & Dongxiao Zhang[1,13] ✉

The stability of particle assemblies is strongly affected by particle shape, yet definitive laws describing key properties, such as the mean contact number and apparent friction coefficient, remain elusive. Using X-ray computed tomography and discrete element simulations, we study 70 assemblies of 3D frictional particles. Once properly rescaled, our data collapse onto master curves, revealing linear relationships linking particle shape to these properties for short-axis particles below certain crossover points. These data suggest that the scaling behavior for the mean contact number can be maintained at lower sphericity than the apparent friction coefficient, indicating different sensitivity of the system's structural versus mechanical properties to particle shape. Through analyzing elongated particles beyond the crossover points, we find that while particle elongation increases the contact number, it has limited effects on improving mechanical stability. This insight, along with the law, paves the route towards optimizing granular packing via manipulating particle shape.

Granular materials are ubiquitous in our daily lives, encompassing a diverse range of substances that are essential in pharmaceuticals[1], agriculture[2], construction[3], and manufacturing[4]. To understand a basic particle assembly, consider releasing many particles above a flat surface. As they accumulate, these particles come into contact and attempt to balance gravity with inter-particle effective interactions like friction and adhesion[5–8]. This balance leads to the formation of a near-conical heap. When this balance is disrupted, the dynamic process can trigger critical behaviors, such as avalanches, until a new stable angle is established[9–11].

Important bulk properties, such as the mean contact number (Z) and the apparent friction coefficient ($\mu = \tan(\theta)$, where θ is the mean angle of repose that defines the slope of the heap surface relative to the horizontal surface; see Supplementary Note 1), are commonly used to describe the structural and mechanical stability of the formed assembly. These properties, largely affected by particle size and shape[12], have been extensively studied in spherical particles, with factors including inter-particle friction coefficient[13–15], surface roughness[16], moisture content[17], Young's modulus[18], and cohesive-to-gravitational force ratio[19]. However, the behavior of non-spherical particles still has to be fully understood. Extending theories for spherical particles[19,20] to predicting non-spherical particle systems can be challenging[21–25]. This is due to the complex contact and flow patterns[26,27] that non-spherical particles can form.

Shape parameters shall be properly chosen when describing said patterns, such as angularity[12], orientation[28], blockiness[29], aspect ratio[30], roundness[31–33], and sphericity[34]. Among these parameters, the most effective practical approaches to describing the overall shapes of the particles are the aspect ratio and sphericity (or asphericity). Prior studies have mainly focused on how the aspect ratio impacts Z and θ phenomenologically[35–37].

[1]School of Environmental Science and Engineering, Southern University of Science and Technology, Shenzhen, China. [2]National Center for Applied Mathematics Shenzhen (NCAMS), Southern University of Science and Technology, Shenzhen, China. [3]Institute of Major Scientific Facilities for New Materials, Southern University of Science and Technology, Shenzhen, China. [4]Shenzhen Key Laboratory of Natural Gas Hydrate, Southern University of Science and Technology, Shenzhen, China. [5]Academy for Advanced Interdisciplinary Studies, Southern University of Science and Technology, Shenzhen, China. [6]School of Chemistry and Molecular Engineering, East China University of Science and Technology, Shanghai, China. [7]School of Sustainable Chemical, Biological and Materials Engineering, University of Oklahoma, Norman, OK, USA. [8]Departments of Physics, Southern University of Science and Technology, Shenzhen, China. [9]Technology Development Center, Kingfa Science and Technology Co., LTD., Guangzhou, China. [10]Department of Mechanical and Energy Engineering, Southern University of Science and Technology, Shenzhen, China. [11]National Research Center of Pumps, Jiangsu University, Zhenjiang, China. [12]Helmholtz Institute Erlangen-Nürnberg for Renewable Energy (IET-2), Forschungszentrum Jülich, Erlangen, Germany. [13]Eastern Institute for Advanced Study, Eastern Institute of Technology, Ningbo, China. ✉e-mail: fand@sustech.edu.cn; zhujl@sustech.edu.cn; dzhang@eitech.edu.cn

However, the aspect ratio has been either defined as a 2D parameter[21] or a quasi-3D parameter[36], and is thus believed to fail to fully capture the geometric characteristics of 3D particles. For example, particles of different shapes—such as cubical, cylindrical, and spherical ones—may all have the aspect ratio of 1, yet their sphericities differ significantly from 0.81 to 1[34]. For studies that have examined sphericity, they have mainly focused on 2D or 3D *frictionless* particles: These findings have suggested that in a 2D system, a 2D asphericity, defined as $\mathcal{A}_{2D} = p^2/4\pi A$ (where p is particle perimeter, and A is particle surface area), can be a universal descriptor for both Z and packing fraction (ϕ) at jamming onset for different particle shapes, as observed in numerical experiments, although the expression for describing such universal behaviors has yet to be reported[38]. In a 3D system, a 3D asphericity, defined as $\mathcal{A}_{3D} = 1 - (4\pi)^{1/3}(3V)^{2/3}/A$ (where V is particle volume), when used alone, has been reported that cannot determine neither Z nor ϕ, but should be combined with an aspect ratio, defined as $\mathcal{B} = d_1 d_3/d_2^2$ (where d_1, d_2, and d_3 are the lengths of the primary axes of the particle, and $d_1 < d_2 < d_3$)[36]. Therefore, the law for 3D non-spherical particles, whether frictionless or frictional ones, with respect to particle shape parameters, remains unidentified. This gap in knowledge naturally leads us to question how particle shape determines the mean contact number and further the apparent friction between particles, as reflected by the mean angle of repose.

To identify reliable laws governing the bulk properties of 3D non-spherical, frictional particles, it is necessary to perform a systematic analysis that should incorporate particle-scale experimental and simulation results of particles with both 2D and 3D shape parameters. Here, we study particles dispensed onto a rough tray via a fixed funnel using X-ray computed tomography (CT) and discrete element method (DEM) simulations. After validating our simulation method against experimental data, we simulate 70 systems, each containing 40,000 identical particles, by varying the shape of the particles at a fixed particle volume. Our analysis reveals a linear scaling law linking particles' inverse sphericity and aspect ratio to the bulk properties (i.e., Z and μ) across systems of various particle shapes. We further discuss how such scaling phenomena enhance our understanding of the stability of the non-spherical particle packing.

Results

Experiments

To directly measure the contact number and apparent friction of non-spherical particles, we prepared particle samples using a high-resolution 3D printer with a layer thickness of 0.08 mm (see the Methods section for printing details). We printed six particle shapes, including sphere, sphero-cylinder, sphero-polygon, and hexagonal prism ones, each with an equivalent diameter of 5 mm. For each shape, approx. 2000 particles were printed using polyamide 12 (PA12) powders. These particles vary in aspect ratio of $\lambda = 1$ and 10 and in sphericity from $\Phi = 1$ to 0.54 (see our definitions of λ and Φ in the Methods section).

To quantify Z, we adopted the X-ray CT scanning technique, similar to the method outlined in a recent study[27]. We released all particles of the same shape into a 3D-printed, open-top, cubic container made of PLA polymer. The particle-filled container was then scanned through the scanner (with a spatial resolution of 26.34 μm), as shown in Fig. 1a and Supplementary Fig. 1. Based on the scanned images, we reconstructed a 3D cubic packing of the particles. To minimize the boundary effect induced by the container walls, we extract a cubic sub-volume from the scanned volume, as shown in Fig. 2. Finally, we estimated Z within the sub-volume using the procedure described in the Methods section.

To estimate μ, we released particles of each shape through a fixed funnel (with a 14 cm trunk length, 6 cm top diameter, 2.5 cm bottom diameter) positioned 5 cm above a tray covered with sack paper. The use of sack paper yields a friction coefficient between the particles and the sack paper of approx. 0.7[39]. Such high roughness allows for the efficient formation of a stable conical structure of particle assemblies, as shown in Fig. 1b. We calculated μ by analyzing the slope of the assembly's profile at the static angle of repose (θ), i.e., $\mu = \tan(\theta)$. To ensure the reliability of our findings, we replicated each experiment three times, calculating the mean from these measurements (see detailed procedure in the Methods section).

Numerical simulations

To numerically simulate the experiments, we conducted DEM simulations using the same parameters as those in our laboratory experiments, and generated particle packs and repose assemblies for the above particle shapes, as shown in Fig. 2 (see detailed contact models in the Methods section). In each simulation, particles were released at a constant mass velocity of 0.09 kg $\cdot$ s^{-1} for 4 s, generating 2000 identical particles. The released particles firstly collide with the tray and then cease to flow due to particle-tray friction. This mechanism is followed by later released particles that interact with the accumulated mass, finding their proper settling position until movement ceases. The final particle assembly is considered stable when the mean translational velocity of all particles decreases to < 0.001 m $\cdot$ s^{-1} and the mean rotational velocity to < 1 rad $\cdot$ s^{-1}. These conditions are met at ≈ 10 s for all cases considered. We estimated Z and θ following the same procedure as in our experiments.

To show the effectiveness of our numerical approach, we compare the simulation against the experimental results, as shown in Fig. 3a, b. The results show that for particles with $\lambda = 1$, a high degree of agreement is observed; and for particles with $\lambda = 10$, more variations are observed, suggesting a more complex contact pattern and anisotropy in particle orientation for elongated particles. To further validate our simulations, we examined the statistical distributions of the orientation angle of particles, and the comparisons are

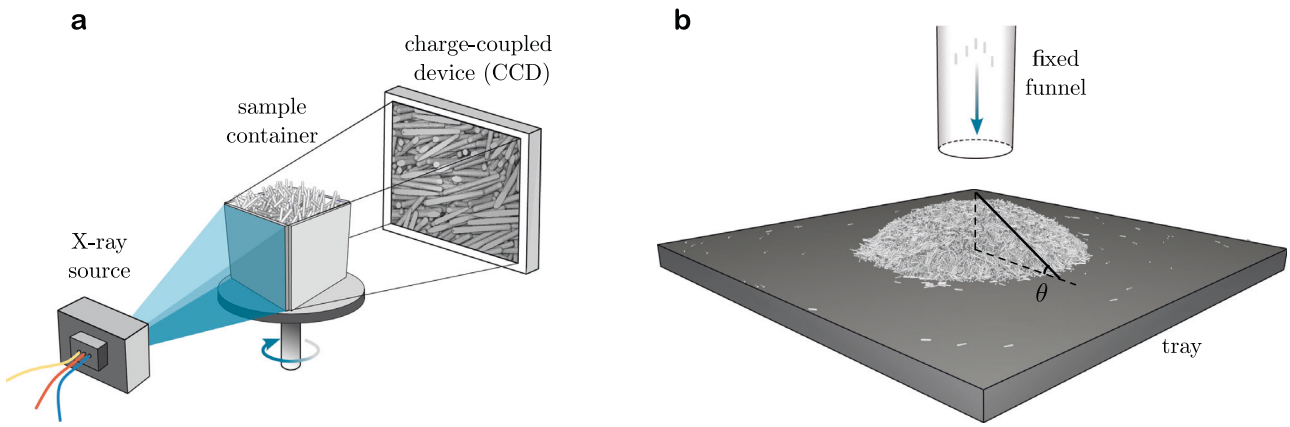

Fig. 1 | Experimental and simulation configurations for particle packing and heap. a X-ray CT scan of a cubic container filled with cylindrical particles, each with an aspect ratio (λ) of 10. **b** Schematic of the particle release process through a fixed funnel onto a rough tray, applicable to both experimental and simulation setups. When the system becomes stable, the mean angle of repose (θ) is measured.

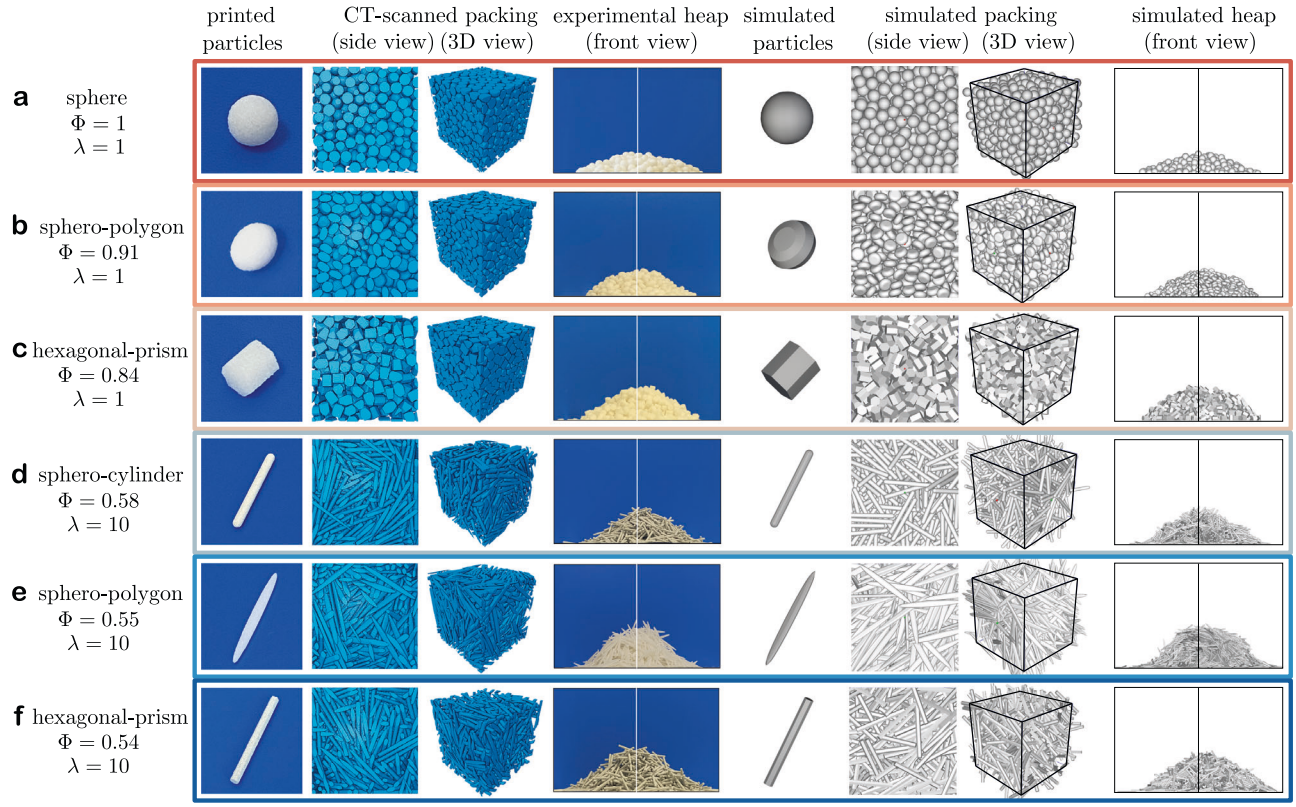

Fig. 2 | Comparisons between the experimental and simulated particle packing and static angle of repose for various particle shapes. The shapes included for comparisons are (**a**) sphere, (**b**) short-axis sphero-polygon, (**c**) short-axis hexagonal-prism, (**d**) elongated sphero-cylinder, (**e**) elongated sphero-polygon, and (**f**) elongated hexagonal-prism. Shown from left to right are the following: 3D-printed PA12 particles, μCT-scanned images of the particle packing in the cube container from a side view and a 3D view, repose of particles on the rough tray, DEM configurations of the simulated particle, simulated particle packing of the particle packing in the cube container from a side view and a 3D view, and simulated repose of particles.

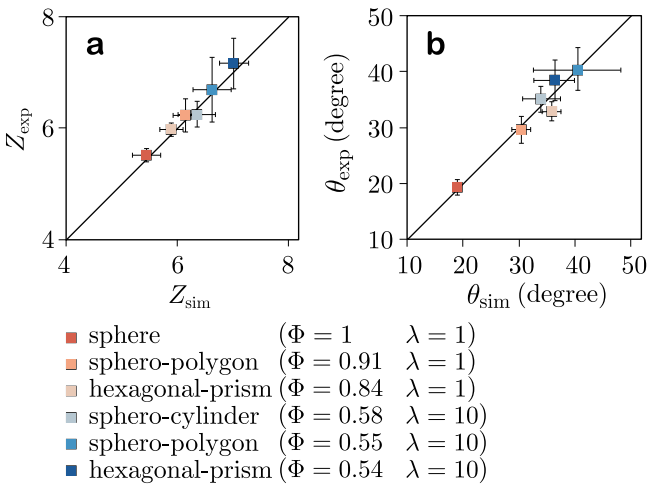

Fig. 3 | Comparisons between experimental and simulated results for 2000 particle samples. Subfigures (**a**, **b**) show Z and θ, respectively. The colors of the symbols correspond to those depicted in Fig. 2. The error bars denote ± 1 the standard deviation of the mean.

shown in Supplementary Fig. 3. Consequently, these comparisons validate that our simulation models are effective in reproducing realistic cubic packing and heaps, which enables us to study the impact of particle shapes by simulating systems with a broad range of shapes.

Therefore, we extended our simulations to include 70 shapes of particles across seven shape families, including sphero-cylinder, ellipsoid, sphero-polyhedron, sphero-polygon, polyhedron, cylinder, and hexagonal-prism ones, with $1 \le \lambda \le 10$ and $0.81 \le \Phi \le 1$ (see all particle geometries in Supplementary Fig. 2). This selection allows us to achieve a wide range of particle primary axis lengths, from 1.37 mm to 27.3 mm (see Supplementary Table 1). To ensure a consistent overall volume of particle assemblies, the particles across all lengths were adjusted to have an equivalent spherical diameter of 5 mm. In each simulation, particles were released at a constant mass velocity of 1.64 kg · s^{-1} for 4 seconds, generating 40,000 identical particles. Using one of the standard packing preparation protocols[12,19,40], we achieve packing fractions from 0.287 to 0.574, aligning with prior experimental trends[41–43] (see detailed comparisons in Supplementary Fig. 4). The following analysis is based on the simulations of the 70 systems as described above.

Scaling relationships of Z, μ, and Φ

We first present the simulated Z and μ along with the surface area (A) of the studied particle, as shown in Fig. 4a, b. These data show that: (1) Both Z and μ increase with A with crossover points at intermediate A values, denoted as the crossover surface area $A_{c|Z}$ and $A_{c|\mu}$, respectively. (2) The data of Z and μ exhibit a greater divergence beyond the crossover points, as indicated by larger error bars, compared to the regions below these points.

To further examine the relationships between dimensionless shape parameters and Z and μ, we compute particles' sphericity (Φ) and aspect ratio (λ). Our data suggest that both Z and μ increase with the inverse sphericity ($1/\Phi$), as shown in Fig. 4c, d. Such relationships are consistent with their relationships to A, due to the definition of $1/\Phi \equiv A/A_{\Phi=1}$, where $A_{\Phi=1}$ is a constant that denotes the surface area of the equivalent sphere whose $\Phi = 1$. The data also indicate that both Z and μ increase with λ, as shown in Fig. 4e, f. However, when $\lambda \to 1$ and $1/\Phi \to 1$, the data points associated with λ are more scattered, as compared to those with $1/\Phi$. Therefore, compared to λ, $1/\Phi$ ostensibly appears to be a more suitable

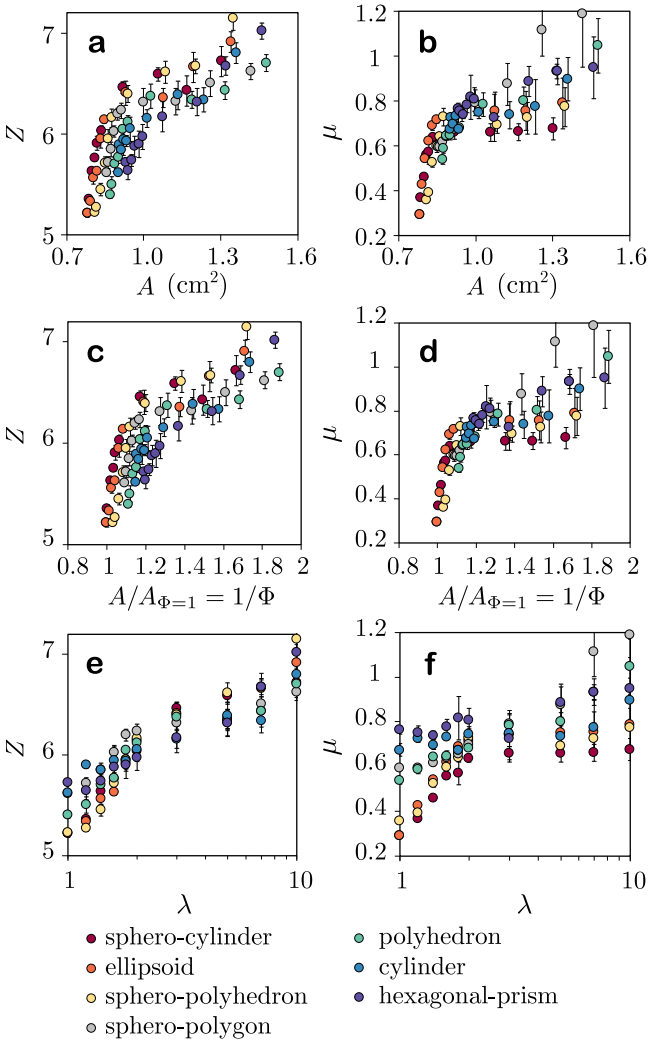

Fig. 4 | Simulated Z, μ, and shape descriptors. Relationships between Z and (**a**) surface area (A), (**c**) inverse sphericity ($1/\Phi$), and (**e**) aspect ratio (λ). Relationships between μ and (**b**) A, (**d**) $1/\Phi$, and (**f**) λ for seven particle shape families, with $1 \le \lambda \le 10$. The error bars denote ± 1 the standard deviation of the mean.

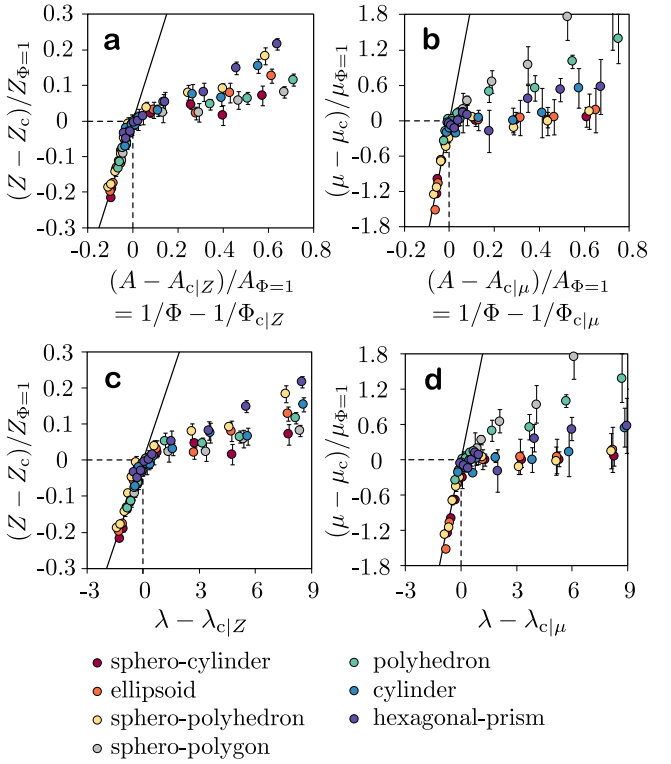

Fig. 5 | Normalized scaling of Z, μ and shape descriptors. Relationships between the normalized mean contact number, $(Z - Z_c)/Z_{\Phi=1}$, and: (**a**) the normalized particle surface area, $(A - A_{c|X})/A_{\Phi=1}$, (equivalent to $1/\Phi - 1/\Phi_{c|Z}$), and (**c**) the-difference between the aspect ratio, λ, and the crossover value, λ_c. Relationships between normalized apparent friction coefficient, $(\mu - \mu_c)/\mu_{\Phi=1}$, and: (**b**) $1/\Phi - 1/\Phi_{c|Z}$, and (**d**) $\lambda - \lambda_c$. In all subfigures, the location (0, 0) corresponds to the crossover point that determines the crossover values of $X = X_c$, $\Phi = \Phi_{c|X}$, and $\lambda = \lambda_{c|X}$. The solid lines show the analytical results of Eq. (1) with $\beta_Z = 2$ in **a** and those with $\beta_\mu = 20$ in (**b**), as well as the analytical results of Eq. (2) with $\beta_\lambda = 13$ and $\beta_Z = 2$ in (**c**), and those with $\beta_\lambda = 13$ and $\beta_\mu = 20$ in (**d**), respectively. The error bars denote ± 1 the standard deviation of the mean. See respective plots in Supplementary Fig. 5.

descriptor (while in the following section, we show λ can be a good candidate under a geometric constraint using Eq. (4)).

Accordingly, we first examine $1/\Phi$ to identify a possible scaling relationship between particle shape and Z and μ. We identify the relationship as follows:

$$\frac{X - X_c}{X_{\Phi=1}} = \beta_X \cdot \left(\frac{1}{\Phi} - \frac{1}{\Phi_{c|X}}\right), \tag{1}$$

where X denotes either Z or μ. Equation (1) essentially describes that the excess of X over X_c is directly proportional to the excess of A over $A_{c|X}$, with both excesses normalized to the values of the equivalent sphere; this relationship is then simplified to the change in the inverse of Φ from its crossover value $\Phi_{c|X}$ by using the definition of Φ, i.e., $(A - A_{c|X})/A_{\Phi=1} \equiv 1/\Phi - 1/\Phi_{c|X}$. The coefficient β_X is a constant that establishes the linear relationship between these normalized changes. Indeed, as shown in Fig. 5a for $X = Z$ and Fig. 5b for $X = \mu$, respectively, the normalized data across different particle shape families properly collapse into two master lines, as described by Eq. (1).

Scaling relationships of Z, μ, and λ

Building on the above analysis, we have identified the inverse sphericity ($1/\Phi$) as a key determinant of X. Considering that numerous studies[35,44–48] have focused on λ as the key shape parameter, we wonder if it is possible to reconcile these two approaches by expressing λ as a function of $1/\Phi$. Since all particles we have considered have equal short axes, specifically $d_1 = d_2 = d$, the aspect ratio of $\lambda = d_3/d$ may effectively represent the studied particle shape. Through analysis of our particle geometries, we observe similar correlations between Φ and λ across seven distinct shape families, as shown in Fig. 6a (note that this observation may not be applicable to particles with $d_1 \neq d_2$). We further identify that the correlations can be normalized to exhibit a seemingly universal trend, as described in Eq. (2). The universality is established by fitting all the simulated data across different shapes to Eq. (2), with the results shown in Fig. 6b.

$$\lambda - 1 = \beta_\lambda \cdot \left(\frac{1}{\Phi} - \frac{1}{\Phi_{\lambda=1}}\right), \tag{2}$$

where $\Phi_{\lambda=1}$ represents the sphericity of the particle that has three equal axes, i.e., $d_1 = d_2 = d_3$ (or $\lambda = 1$). We find $\Phi_{\lambda=1}$ is a characteristic sphericity for a given particle shape family in that it is a constant for a given family, but differs across families, as presented in Figs. 6c through e. β_λ is the coefficient that establishes the proportionality between λ and $1/\Phi$.

By substituting Eq. (2) into Eq. (1), we derive

$$\frac{X - X_c}{X_{\Phi=1}} = \frac{\beta_X}{\beta_\lambda} \cdot (\lambda - \lambda_{c|X}), \tag{3}$$

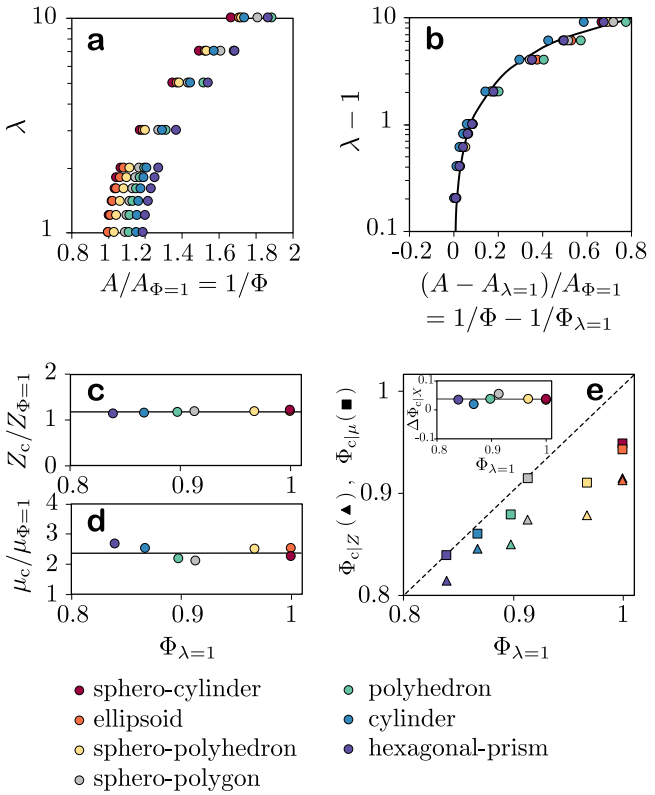

Fig. 6 | Relationships between the crossover parameters and shape descriptors. **a** Relationships between the aspect ratio (λ) and inverse sphericity ($1/\Phi$). **b** Relationships between ($\lambda - 1$) and ($1/\Phi - 1/\Phi_{\lambda=1}$). The solid line shows the analytical data of Eq. (2) with $\beta_\lambda = 13$. (**c**, **d**) show the relationships between scaled μ and $\Phi_{\lambda=1}$, and scaled Z and $\Phi_{\lambda=1}$, respectively. **e** Relationships between $\Phi_{c|Z}$, $\Phi_{c|\mu}$, and $\Phi_{\lambda=1}$. The inset shows the relationships between the difference $\Delta\Phi_{c|X}$ ($= \Phi_{c|\mu} - \Phi_{c|Z}$) and $\Phi_{\lambda=1}$. The dashed line in is the 45 ° line. Horizontal lines in (**c**–**e**) indicate the respective average values.

which indicates that there exists a crossover value of the aspect ratio for X, expressed in

$$\lambda_{c|X} = 1 - \beta_\lambda \cdot \left(\frac{1}{\Phi_{\lambda=1}} - \frac{1}{\Phi_{c|X}}\right), \tag{4}$$

below which the scaling law between X and λ holds.

Based on $\Phi_{c|X}$ values estimated from Figs. 5a and b, we calculate $\lambda_{c|X}$ and show the processed data in Fig. 5c, d. We identify the range of $1.4 \lesssim \lambda_{c|Z} \lesssim 2.3$ and $1.1 \lesssim \lambda_{c|\mu} \lesssim 1.8$ for our 3D frictional particles (we have marked the particle shapes that fall within the crossover ranges in Supplementary Fig. 2), which aligns well with the reported results for 2D & 3D frictionless particles where $\lambda_{c|Z} \lesssim 2$[36,38] and for 2D frictional particles where $1.5 \lesssim \lambda_{c|Z} \lesssim 1.8$[49]. Two master lines are predicted by Eq. (3) and the prior estimated β_X and β_λ. The accurate prediction of the trends in the simulated data, as shown in Figs. 5c and d, confirms the proposed mapping from Φ to λ. See further validation of the theory through our experiments and those reported in the literature[2,44,50–54] in Supplementary Figs. 6 and 7.

The above analysis reveals that, for the packing protocol considered here, a set of crossover parameters, X_c and $\Phi_{c|X}$, is sufficient to describe the linear relationships between the normalized X, Φ, and λ within the same shape family. To determine X_c, we find that both Z_c and μ_c vary little with $\Phi_{\lambda=1}$ and can be treated as constants, as demonstrated in Figs. 6c and d. In contrast, the challenge lies in the determination of $\Phi_{c|X}$ that requires data fitting. Given that $\Phi_{\lambda=1}$ is more easily obtainable from experiments, it is desirable to derive $\Phi_{c|X}$ from $\Phi_{\lambda=1}$. Indeed, we find that $\Phi_{c|X}$ is positively correlated with $\Phi_{\lambda=1}$, which facilitates the estimation of $\Phi_{c|X}$ through $\Phi_{\lambda=1}$ (and also facilitates the estimation of $\lambda_{c|X}$); moreover, when $\Phi_{\lambda=1} < 0.93$, $\Phi_{c|\mu}$ can be approximated as $\Phi_{\lambda=1}$, as suggested in Fig. 6e. Consequently, once $\Phi_{\lambda=1}$ is determined, both Z and μ can be estimated either by using Φ with Eq. (1), or by using λ with Eq. (3).

Deviation from scaling relationships

For the packing protocol under consideration, beyond the crossover values of $\Phi_{c|Z}$, $\lambda_{c|Z}$, $\Phi_{c|\mu}$, and $\lambda_{c|\mu}$, the data of Z and μ begin to deviate from the original linearity, as shown in Fig. 5. Due to the large error bars, which reflected the increased anisotropy of the packing at high aspect ratios[55], we cannot clearly identify a universal pattern of Z and μ with particle shape. Although not deterministic, the trend of the data is sufficient to indicate different patterns in Z and μ with respect to the shape parameters: Of all particle shapes simulated here, we find that for Z, their values tend to continuously increase with the λ and $1/\Phi$ albeit at a lower rate than that before the crossover points. In contrast, μ values may not consistently increase as their corresponding Z. For instance, μ values of sphero-polygon and polyhedron particles continue to increase; while μ values of sphero-cylinder, ellipsoid, sphero-polyhedron, cylinder, and hexagonal-prism particles tend to saturate, aligning with observations from other studies[9,49].

Discussion

Consider that Z and μ are different physical quantities of particle assemblies, a structural versus a mechanical one, respectively. It is expected that they would exhibit different sensitivities to particle shape, such as $\Phi_{c|Z} \neq \Phi_{c|\mu}$. Our data indeed show that $\Phi_{c|Z} < \Phi_{c|\mu}$ (Fig. 6e), suggesting that the linear relationship for Z is maintained at lower sphericity than that for μ (namely, the linearity of Z is observed to diminish at a higher inverse sphericity compared to μ in Fig. 4c, d).

This difference can be attributed to the nature of these two quantities. μ, which reflects the material's overall shear resistance, is influenced by both the number of contacts and the mechanisms of force transmission within the contact network[45]. As Φ decreases, the surface area increases at a fixed particle volume, and the apparent friction is expected to increase. Once Φ falls below $\Phi_{c|\mu}$, the reorganization of contact force chains and the anisotropy of the contact network[47] alter the pattern of increase in μ, which disrupts its original linear scaling. In contrast, as surface area increases, the formation of additional contact points persists, which maintains a steady linear increase in Z. Therefore, when $\Phi_{c|Z} < \Phi < \Phi_{c|\mu}$, μ deviates its initial linearity while particle shape continues to linearly impact Z. This observation underscores the distinct sensitivity of the system's structural versus mechanical properties to particle shape. The fact that $\Delta\Phi_{c|X} = \Phi_{c|\mu} - \Phi_{c|z}$ remains nearly constant, as shown in the inset of Fig. 6e, may imply that these differences in sensitivity could be independent of the specific type of particle shape.

Beyond the crossover regions, our data do not show a universal relationship between both Z, μ and shape parameters. This suggests that the mechanical structure of the system becomes more complex that can no longer be dictated by a single shape parameter. The complexity also reflects in the different progression of Z and μ with λ and $1/\Phi$, i.e., the former continuously increases while the latter could potentially reach a saturation state. This difference reflects the different impact of particle shape on contact versus friction. This further indicates that as $\lambda \gg \lambda_{c|X}$ and $\Phi \ll \Phi_{c|X}$, deviations from a spherical shape contribute to the increase of contact points, but are limited in improving the mechanical stability of the assembly of certain types of particle shapes.

In summary, we have shown the scaling in the contact number (Z) and apparent friction coefficient (μ) across 3D assemblies of particles of nearly-equiaxed through elongated shapes. When shape parameters, both sphericity (Φ) and aspect ratio (λ), are within their specific crossover thresholds ($0.95 \lesssim \Phi \leq 1$ and $1 \leq \lambda \lesssim 2.3$), there is such a consistently linear dependence of these bulk properties on particle shape. The nuanced differences in the crossover shape parameters suggest varying sensitivities of particle shape to structural versus mechanical properties, independent of specific particle shape types. This insight, along with the reported linear expression, shall

permit targeted control over the mechanical stability in packing of these short-axis particles, particularly that prepared using a protocol similar to ours. However, controlling the stable packing of highly elongated particles remains challenging, because the system's structural and mechanical properties are no longer governed by a single shape descriptor beyond those crossover thresholds. Consequently, whether universal scaling emerges for highly elongated particles and how it could potentially saturate remain outstanding questions.

Supplementary Information includes an additional note about the angle of repose and results, along with references[2,36,38,41–44,49–54,56].

Methods

Characterization of particle shape

To accurately measure the lengths of a 3D particle along its principal axes, denoted as d_1, d_2, and d_3, we aligned the particle along the coordinate system's axes, x, y, and z, respectively. The particle's most elongated axis was aligned along the z-axis, while the remaining principal axes d_1 and d_2 were determined along the x- and y-axis, respectively. For simplicity, we modeled all particles of $d_1 = d_2 = d$.

The aspect ratio (λ) was estimated as the length ratio of the most elongated axis to the short axis, as given by $\lambda \equiv d_3/d$, where $\lambda \geq 1$ for all shapes of particles. The sphericity (Φ) was calculated as the ratio of the surface area ($A_{\Phi=1}$) of the sphere with the same volume as the particle, namely the equivalent sphere, to the particle's actual surface area (A), as expressed in $\Phi \equiv A_{\Phi=1}/A$[34], and $\Phi \leq 1$ for all shapes of particles.

3D printing of particles

An HP Jet Fusion 540 (MJF) printer was utilized to fabricate the designed 3D particles using polyamide 12 (HP PA12), which has a mean powder particle size of 52 μm. All the samples were placed along the vertical direction to reduce the step effect associated with layer-by-layer printing. After printing, the samples underwent an abrasive blasting treatment to remove the excess powder adhering to the surface, ensuring high surface consistency. The polished PA12 particles yield an inter-particle friction coefficient of approx. 0.43[57]. Additionally, a container with dimensions of 55 mm × 55 mm × 70 mm was designed to match the CT scan requirements and to hold the particles. This container was fabricated using PLA polymer with an FDM printer (Bambu Lab X1, China).

μCT experiments

X-ray CT (nanovoxel 3432E, Sanying Precision Instruments Co., Ltd.) was used to acquire 3D images and quantify the contact numbers of different particle packing in a 50 mm × 50 mm × 50 mm cubic container. This method has been recently proven successful in revealing contacting force chains in 3D assemblies of non-spherical particles[27]. The X-ray CT was operated at 150 kV with a current of 60 μA, with a source-to-object distance of 29.9 cm and a source-to-detector distance of 56.1 cm. Images were acquired using 1080 projections with an exposure time of 0.9 s, resulting in a reconstructed 3D model with dimensions of 2940 × 2940 × 2304 voxels, with a spatial resolution (voxel size) of 26.34 μm. The number of projections was chosen to optimize the image signal-to-noise ratio while not significantly increasing the acquisition time.

Avizo software (version 2022.1, Thermo Fisher Scientific Inc.) was utilized to generate 3D models of particle packing and evaluate their contact numbers. The raw images were subjected to filtering processes, including anisotropic diffusion for noise reduction and unsharp masking to enhance edge contrast. Subsequently, the filtered images underwent binarization transformation to identify particles, converting grayscale images into binary ones through interactive thresholding. Each particle was segmented into a separate object using the watershed algorithm. Finally, the mean contact numbers were determined using neighbor count measurements from label analysis. The cutoff distance, which represents the distance from the boundary of the considered label to the candidate neighbor labels, was set to 0.2 mm. This specific threshold was chosen to align with the layer thickness limitations inherent in our 3D printing technology, ensuring that the DEM model accurately reflect the physical constraints of the printing process. Additionally, the minimum overlap was set to 0%, ensuring retention of any neighbor that has at least one voxel within the search area.

DEM simulations

Our simulation setup involves releasing particles through a fixed funnel above a rough tray that serves as an impenetrable boundary with an open side. The fixed funnel was positioned as shown in Fig. 1b and has a Young's modulus of 6.5×10^{10} Pa. The particles were generated and released with random orientations to ensure that the simulations accurately reflect our experimental conditions. Particle properties, such as their density (2.5 g · cm^{-3}), Young's modulus ($E = 1 \times 10^7$Pa), Poisson's ratio ($\nu = 0.3$), coefficient of restitution ($\varepsilon = 0.2$), as well as the friction coefficient among particles ($\mu = 0.5$) and that between the particles and the tray ($\mu = 0.7$), were set as constant for all systems examined. We neglected cohesion between particles, as their sizes are relatively large: all having an equivalent diameter of 5 mm, which is beyond the typical range where cohesion significantly impacts behavior[19].

The normal contact forces were simulated using the Hertzian spring dashpot model[58], which includes nonlinear elastic and damping components that depend on the overlap of the Hertzian model, as described in Eq. (5).

$$F_n = \hat{K} s_n^{\frac{3}{2}} + \hat{C} s_n^{\frac{1}{4}} \dot{s}_n, \tag{5}$$

where s_n is the contact normal overlap, $\dot{s}_n$ is the time derivative of s_n, $\hat{K} = \frac{4}{3} E^* \sqrt{R^*}$ is the stiffness coefficient, $E^* = E/2(1-\nu^2)$ is the reduced Young's modulus, R^* is the equivalent radius of the contacting particles, $\hat{C} = 2\eta_n \sqrt{m^* \hat{K}}$ is the damping coefficient[59], $m^* = m/2$ is the effective mass of contacting particles, m is the particle mass, $\eta_n = \frac{\sqrt{5}}{2}\eta$ is the damping ratio[60], and η is the damping ratio in the linear spring dashpot model, which is derived from ε using $\ln \varepsilon = -\frac{\eta}{\sqrt{1-\eta^2}} \left(\pi - \arctan \frac{2\eta\sqrt{1-\eta^2}}{1-2\eta^2} \right)$[61].

For the tangential contact forces, we adopted the Mindlin-Deresiewicz model[62], as presented by Eq. (6).

$$\mathbf{F}_\tau = -\mu F_n \cdot \left(1 - \varsigma^{\frac{3}{2}}\right) \frac{\mathbf{s}_\tau}{|\mathbf{s}_\tau|} + \eta_\tau \sqrt{\frac{6\mu m^* F_n}{s_{\tau,\max}}} \varsigma^{\frac{1}{4}} \dot{\mathbf{s}}_\tau, \tag{6}$$

where $\varsigma = 1 - \min(|\mathbf{s}_\tau|, s_{\tau,\max})/s_{\tau,\max}$, $\mathbf{s}_\tau$ is the tangential relative displacement at the contact, $\dot{\mathbf{s}}_\tau$ is the tangential component of the relative velocity at the contact, $s_{\tau,\max} = \mu(2-\nu)/(2-2\nu) \cdot s_n$ is the maximum relative tangential displacement before particles start to slide, and $\eta_\tau = -\ln \varepsilon / \sqrt{\ln^2 \varepsilon + \pi^2}$ is the tangential damping ratio.

The simulations were implemented on the commercial software Rocky DEM (version 3.1), which guarantees the high accuracy and reliability of our findings. These simulations were further accelerated by leveraging the computational power of an NVIDIA GeForce RTX™ 3080 GPU. To efficiently monitor the simulation over time, simulation results were recorded every 0.01 seconds.

Data extraction

To estimate the mean contact number between particles, we adopted the definition of $Z = 2N_c/N_p$[36], where N_c is the number of particle contacts, and N_p is the total number of particles within the analysis region. In our experiments, we determined Z within the sub-volume of the cubic container. In our simulations, we first analyzed Z in the largest cube inscribed by the assembly; then, by gradually reducing the cube size, we obtained a series of smaller cubic regions that contain fewer and fewer particles, then from the analysis of these cubes, we identified a representative Z for subsequent analysis.

To determine θ of the assembly and ensure the consistency of the estimate, we adopted the following method. We first determined the center of mass of the heap's base and then identified the heap's center line, which is the line that crosses the center of mass and is perpendicular to the base. We

then created a plane that intersects the center line and duplicate this plane to generate a total of six planes, each spaced 30 degrees apart from its neighbors and all intersecting the center line. We subsequently projected the heap onto these six planes and recorded the resulting twelve 2D profiles. Then, each profile was fitted to the nonlinear equation described in ref. 63, from which the inflection point and its slope were determined. This process was applied to all profiles to estimate their respective angles of repose. Finally, the mean angle of repose (θ) and the standard deviation were calculated.

Data availability

The authors declare that all the relevant data are available within the paper and its Supplementary Information file or from the corresponding author upon reasonable request.

Received: 26 June 2024; Accepted: 17 February 2025;
Published online: 26 February 2025

References

1. Freireich, B., Ketterhagen, W. R. & Wassgren, C. Intra-tablet coating variability for several pharmaceutical tablet shapes. *Chem. Eng. Sci.* **66**, 2535–2544 (2011).
2. Mousaviraad, M., Tekeste, M. & Rosentrater, K. A. Calibration and validation of a discrete element model of corn using grain flow simulation in a commercial screw grain auger. *Trans. ASABE.* **60**, 1403–1416 (2017).
3. Metcalf, J. R. Angle of repose and internal friction. *Int. J. Rock Mech. Min. Sci. & Geomech. Abstr.* **3**, 155–161 (1966).
4. Jaeger, H. M., Shinbrot, T. & Umbanhowar, P. B. Does the granular matter? *Proc. Natl. Acad. Sci. U.S.A.* **97**, 12959–12960 (2000).
5. Richard, P. et al. Rheology of confined granular flows: scale invariance, glass transition, and friction weakening. *Phys. Rev. Lett.* **101**, 248002 (2008).
6. Bérut, A., Pouliquen, O. & Forterre, Y. Brownian granular flows down heaps. *Phys. Rev. Lett.* **123**, 248005 (2019).
7. Castellanos, A., Valverde, J. M. & Quintanilla, M. A. S. Physics of compaction of fine cohesive particles. *Phys. Rev. Lett.* **94**, 075501 (2005).
8. Wilson-Whitford, S. R., Gao, J., Roffin, M. C., Buckley, W. E. & Gilchrist, J. F. Microrollers flow uphill as granular media. *Nat. Commun.* **14**, 5829 (2023).
9. Frette, V. et al. Avalanche dynamics in a pile of rice. *Nature* **379**, 49–52 (1996).
10. Xing, Y. et al. Origin of the critical state in sheared granular materials. *Nat. Phys.* **20**, 646–652 (2024).
11. Royer, J. R. & Chaikin, P. M. Precisely cyclic sand: self-organization of periodically sheared frictional grains. *Proc. Natl. Acad. Sci. U.S.A.* **112**, 49–53 (2015).
12. Al-Hashemi, H. M. & Al-Amoudi, O. S. B. A review on the angle of repose of granular materials. *Powder Technol.* **330**, 397–417 (2018).
13. Mutabaruka, P., Delenne, J.-Y., Soga, K. & Radjai, F. Initiation of immersed granular avalanches. *Phys. Rev. E* **89**, 052203 (2014).
14. Preud'homme, N., Lumay, G., Vandewalle, N. & Opsomer, E. Numerical measurement of flow fluctuations to quantify cohesion in granular materials. *Phys. Rev. E* **104**, 064901 (2021).
15. Zeng, Z. et al. Equivalence of fluctuation-dissipation and edwards' temperature in cyclically sheared granular systems. *Phys. Rev. Lett.* **129**, 228004 (2022).
16. Pohlman, N. A., Severson, B. L., Ottino, J. M. & Lueptow, R. M. Surface roughness effects in granular matter: influence on angle of repose and the absence of segregation. *Phys. Rev. E* **73**, 031304 (2006).
17. Ileleji, K. E. & Zhou, B. The angle of repose of bulk corn stover particles. *Powder Technol.* **187**, 110–118 (2008).
18. Jiang, Y. et al. Discrete element method–computational fluid dynamics analyses of flexible fibre fluidization. *J. Fluid Mech.* **910**, A8 (2021).
19. Elekes, F. & Parteli, E. J. R. An expression for the angle of repose of dry cohesive granular materials on Earth and in planetary environments. *Proc. Natl. Acad. Sci. U.S.A.* **118**, e2107965118 (2021).
20. Guo, Z. et al. Theoretical and experimental investigation on angle of repose of biomass-coal blends. *Fuel* **116**, 131–139 (2014).
21. Hidalgo, R. C., Szabó, B., Gillemot, K., Börzsönyi, T. & Weinhart, T. Rheological response of nonspherical granular flows down an incline. *Phys. Rev. Fluids* **3**, 074301 (2018).
22. Donev, A. et al. Improving the density of jammed disordered packings using ellipsoids. *Science* **303**, 990–993 (2004).
23. Baule, A., Mari, R., Bo, L., Portal, L. & Makse, H. A. Mean-field theory of random close packings of axisymmetric particles. *Nat. Commun.* **4**, 2194 (2013).
24. Gao, L., Shokouhi, P. & Rivière, J. Effect of grain shape and relative humidity on the nonlinear elastic properties of granular media. *Geophys. Res. Lett.* **50**, e2023GL103245 (2023).
25. Cúñez, F. D., Patel, D. & Glade, R. C. How particle shape affects granular segregation in industrial and geophysical flows. *Proc. Natl. Acad. Sci. U.S.A.* **121**, e2307061121 (2024).
26. Deal, E. et al. Grain shape effects in bed load sediment transport. *Nature* **613**, 298–302 (2023).
27. Li, W. & Juanes, R. Dynamic imaging of force chains in 3D granular media. *Proc. Natl. Acad. Sci. U.S.A.* **121**, e2319160121 (2024).
28. Wang, D. et al. Interplay between spherical confinement and particle shape on the self-assembly of rounded cubes. *Nat. Commun.* **9**, 2228 (2018).
29. Zhao, S., Zhang, N., Zhou, X. & Zhang, L. Particle shape effects on fabric of granular random packing. *Powder Technol.* **310**, 175–186 (2017).
30. Sarate, P. S., Murthy, T. G. & Sharma, P. Column to pile transition in quasi-static deposition of granular chains. *Soft Matter* **18**, 2054–2059 (2022).
31. Gui, N., Yang, X., Tu, J. & Jiang, S. Effect of roundness on the discharge flow of granular particles. *Powder Technol.* **314**, 140–147 (2017).
32. Zheng, J. & Hryciw, R. D. Traditional soil particle sphericity, roundness and surface roughness by computational geometry. *Geotechnique* **65**, 494–506 (2015).
33. Fu, J.-J., Chen, C., Ferellec, J.-F. & Yang, J. Effect of particle shape on repose angle based on hopper flow test and discrete element method. *Advances in Civil Engineering* **2020**, 8811063 (2020).
34. Li, T., Li, S., Zhao, J., Lu, P. & Meng, L. Sphericities of non-spherical objects. *Particuology* **10**, 97–104 (2012).
35. Zhou, Z. Y., Zou, R. P., Pinson, D. & Yu, A. B. Angle of repose and stress distribution of sandpiles formed with ellipsoidal particles. *Granul. Matter* **16**, 695–709 (2014).
36. Yuan, Y., VanderWerf, K., Shattuck, M. D. & O'Hern, C. S. Jammed packings of 3D superellipsoids with tunable packing fraction, coordination number, and ordering. *Soft Matter* **15**, 9751–9761 (2019).
37. Landauer, J., Kuhn, M., Nasato, D. S., Foerst, P. & Briesen, H. Particle shape matters–Using 3D printed particles to investigate fundamental particle and packing properties. *Powder Technol.* **361**, 711–718 (2020).
38. VanderWerf, K., Jin, W., Shattuck, M. D. & O'Hern, C. S. Hypostatic jammed packings of frictionless nonspherical particles. *Phys. Rev. E* **97**, 012909 (2018).
39. Fellers, C., Backstrom, M., Htun, M. T. & Lindholm, G. Paper-to-paper friction - paper structure and moisture. *Nord. Pulp Pap. Res. J.* **13**, 225–232 (1998).
40. Philipse, A. P. The random contact equation and its implications for (colloidal) rods in packings, suspensions, and anisotropic powders. *Langmuir* **12**, 5971 (1996).
41. Philipse, A. P., Nechifor, A.-M. & Patmamanoharan, C. Isotropic and birefringent dispersions of surface modified silica rods with a boehmite-needle core. *Langmuir* **10**, 4451–4458 (1994).
42. Thies-Weesie, D. M., Philipse, A. P. & Kluijtmans, S. G. Preparation of sterically stabilized silica-hematite ellipsoids: Sedimentation, permeation, and packing properties of prolate colloids. *J. Colloid Interface Sci.* **174**, 211–223 (1995).

43. Philipse, A. P. & Pathmamanoharan, C. Liquid permeation (and sedimentation) of dense colloidal hard-sphere packings. *J. Colloid Interface Sci.* **159**, 96–107 (1993).
44. Xiao, W. L., Chen, H., Wan, X. Y., Li, M. L. & Liao, Q. X. Influence of shape and particle size distribution on discrete element simulation flow characteristics of granular compound fertilizers. *Appl. Eng. Agric.* **37**, 1169–1179 (2021).
45. Chen, H., Zhao, S. & Zhou, X. DEM investigation of angle of repose for super-ellipsoidal particles. *Particuology* **50**, 53–66 (2020).
46. Zhao, H. Y., An, X. Z., Gou, D. Z., Zhao, B. & Yang, R. Y. Attenuation of pressure dips underneath piles of spherocylinders. *Soft Matter* **14**, 4404–4410 (2018).
47. Dai, B.-B., Yang, J. & Zhou, C.-Y. Micromechanical origin of angle of repose in granular materials. *Granul. Matter* **19**, 24 (2017).
48. Nan, W., Ghadiri, M. & Wang, Y. Analysis of powder rheometry of FT4: Effect of particle shape. *Chem. Eng. Sci.* **173**, 374–383 (2017).
49. Trulsson, M. Rheology and shear jamming of frictional ellipses. *J. Fluid Mech.* **849**, 718–740 (2018).
50. Varnamkhasti, M. G. et al. Some physical properties of rough rice (Oryza Sativa L.) grain. *J. Cereal Sci.* **47**, 496–501 (2008).
51. Itabiyi, O., Adebowale, A. A., Shittu, T. A., Adigbo, S. O. & Sanni, L. O. Effect of ratooning process on the engineering properties of NERICA rice varieties. *Qual. Assur. Saf. Crop. Foods* **8**, 21–31 (2016).
52. Tekeste, M. Z., Mousaviraad, M. & Rosentrater, K. A. Discrete element model calibration using multi-responses and simulation of corn flow in a commercial grain auger. *Trans. ASABE.* **61**, 1743–1755 (2018).
53. Wang, L. J., Li, R., Wu, B. X., Wu, Z. C. & Ding, Z. J. Determination of the coefficient of rolling friction of an irregularly shaped maize particle group using physical experiment and simulations. *Particuology* **38**, 185–195 (2018).
54. Geng, L. et al. Calibration and experimental validation of contact parameters for oat seeds for discrete element method simulations. *Appl. Eng. Agric.* **37**, 605–614 (2021).
55. Delaney, G. W. & Cleary, P. W. The packing properties of superellipsoids. *EPL* **89**, 34002 (2010).
56. Cheng, N.-S. & Zhao, K. Difference between static and dynamic angle of repose of uniform sediment grains. *Int. J. Sediment Res.* **32**, 149–154 (2017).
57. Yu, G. et al. Mechanical and tribological properties of 3D printed polyamide 12 and SiC/PA12 composite by selective laser sintering. *Polymers* **14**, 2167 (2022).
58. Navarro, H. A. & de Souza Braun, M. P. Determination of the normal spring stiffness coefficient in the linear spring–dashpot contact model of discrete element method. *Powder Technol.* **246**, 707–722 (2013).
59. Tsuji, Y., Tanaka, T. & Ishida, T. Lagrangian numerical simulation of plug flow of cohesionless particles in a horizontal pipe. *Powder Technol.* **71**, 239–250 (1992).
60. Antypov, D. & Elliott, J. A. On an analytical solution for the damped Hertzian spring. *Europhys. Lett.* **94**, 50004 (2011).
61. Schwager, T. & Pöschel, T. Coefficient of restitution and linear–dashpot model revisited. *Granul. Matter* **9**, 465–469 (2007).
62. Guo, Y., Wassgren, C., Hancock, B., Ketterhagen, W. & Curtis, J. Validation and time step determination of discrete element modeling of flexible fibers. *Powder Technol.* **249**, 386–395 (2013).
63. Müller, D., Fimbinger, E. & Brand, C. Algorithm for the determination of the angle of repose in bulk material analysis. *Powder Technol.* **383**, 598–605 (2021).

Acknowledgements

We acknowledge financial support from the National Natural Science Foundation of China (No. 42202136, 52288101, 52106092), Natural Science Foundation of Guangdong Province (No. 2023A1515012761), National Key R&D Program of China (No. 2023YFB4603502, 2022YFE0197100), Shenzhen Science and Technology Innovation Commission (No. KQTD20190929172505711), Shenzhen Key Laboratory of Natural Gas Hydrates (No. ZDSYS20200421111201738), Shenzhen Science and Technology Program (No. JCYJ20220530113011027, JCYJ20220818095605012, 202103243001393), the Major Science and Technology Infrastructure Project of Material Genome Big-Science Facilities Platform supported by the Municipal Development and Reform Commission of Shenzhen. D.F. would like to thank for the support of the Pengcheng Peacock Plan. A.S. is grateful to the Asahi Glass Chair of Chemical Engineering at the University of Oklahoma for funding. We also thank Liangliang Huang for providing useful feedback.

Author contributions

D.F. performed numerical simulations and theoretical development. Y.C. and Z.L. conducted μCT experiments under the supervision of P.W., Y.L., and J.Z. J.L. performed additional experiments to determine the angle of repose under the supervision of Y.T. S.Z. prepared the 3D-printed particles under the supervision of J.B. L.Z. provided the commercial software license for DEM simulations. D.F., Y.C., Z.L., C.L., A.S., and P.M. were responsible for analyzing the data. D.Z. secured funding and supervised the overall project. D.F., P.W., A.S., S.Z., P.M., and D.Z. contributed to the writing of the paper.

Competing interests

The authors declare no competing interests.

Additional information

Supplementary information The online version contains supplementary material available at https://doi.org/10.1038/s42005-025-02009-0.

Correspondence and requests for materials should be addressed to Dian Fan, Jinlong Zhu or Dongxiao Zhang.

Peer review information *Communications Physics* thanks Fernando David Cúñez and the other, anonymous, reviewer(s) for their contribution to the peer review of this work.